



CHALMERS
UNIVERSITY OF TECHNOLOGY

Ion Transport Mechanisms via Time-Dependent Local Structure and Dynamics in Highly Concentrated Electrolytes

Downloaded from: <https://research.chalmers.se>, 2025-12-09 00:08 UTC

Citation for the original published paper (version of record):

Andersson, R., Årén, F., Franco, A. et al (2020). Ion Transport Mechanisms via Time-Dependent Local Structure and Dynamics in Highly Concentrated Electrolytes. *Journal of the Electrochemical Society*, 167(14).
<http://dx.doi.org/10.1149/1945-7111/abc657>

N.B. When citing this work, cite the original published paper.

OPEN ACCESS

Ion Transport Mechanisms via Time-Dependent Local Structure and Dynamics in Highly Concentrated Electrolytes

To cite this article: Rasmus Andersson *et al* 2020 *J. Electrochem. Soc.* **167** 140537

View the [article online](#) for updates and enhancements.

239th ECS Meeting

with the 18th International Meeting on Chemical Sensors (IMCS)

ABSTRACT DEADLINE: DECEMBER 4, 2020



May 30-June 3, 2021

SUBMIT NOW →



Ion Transport Mechanisms via Time-Dependent Local Structure and Dynamics in Highly Concentrated Electrolytes

Rasmus Andersson,^{1,z}  Fabian Årén,¹ Alejandro A. Franco,^{2,3,4,5} and Patrik Johansson^{1,4,z} 

¹Department of Physics, Chalmers University of Technology, SE-412 96 Gothenburg, Sweden

²Laboratoire de Réactivité et Chimie des Solides (LRCS), Université de Picardie Jules Verne UMR CNRS 7314, Hub de l'Energie, 80039 Amiens, France

³Réseau sur le Stockage Electrochimique de l'Energie (RS2E), FR CNRS 3459, Hub de l'Energie, 80039 Amiens, France

⁴Alistore-ERI European Research Institute, CNRS FR 3104, Hub de l'Energie, 80039 Amiens, France

⁵Institut Universitaire de France, 75005 Paris, France

Highly concentrated electrolytes (HCEs) are attracting interest as safer and more stable alternatives to current lithium-ion battery electrolytes, but their structure, solvation dynamics and ion transport mechanisms are arguably more complex. We here present a novel general method for analyzing both the structure and the dynamics, and ultimately the ion transport mechanism(s), of electrolytes including HCEs. This is based on automated detection of bonds, both covalent and coordination bonds, including how they dynamically change, in molecular dynamics (MD) simulation trajectories. We thereafter classify distinct local structures by their bond topology and characterize their physicochemical properties by statistical mechanics, giving both a qualitative and quantitative description of the structure, solvation and coordination dynamics, and ion transport mechanism(s). We demonstrate the method by in detail analyzing an ab initio MD simulation trajectory of an HCE consisting of the LiTFSI salt dissolved in acetonitrile at a 1:2 molar ratio. We find this electrolyte to form a flexible percolating network which limits vehicular ion transport but enables the Li⁺ ions to move between different TFSI coordination sites along with their first solvation shells. In contrast, the TFSI anions are immobilized in the network, but often free to rotate which further facilitates the Li⁺ hopping mechanism.

© 2020 The Author(s). Published on behalf of The Electrochemical Society by IOP Publishing Limited. This is an open access article distributed under the terms of the Creative Commons Attribution Non-Commercial No Derivatives 4.0 License (CC BY-NC-ND, <http://creativecommons.org/licenses/by-nc-nd/4.0/>), which permits non-commercial reuse, distribution, and reproduction in any medium, provided the original work is not changed in any way and is properly cited. For permission for commercial reuse, please email: permissions@iopublishing.org. [DOI: 10.1149/1945-7111/abc657]



Manuscript submitted June 22, 2020; revised manuscript received October 21, 2020. Published November 11, 2020.

Supplementary material for this article is available [online](#)

Lithium-ion batteries (LIBs) are today used for powering both mobile electronics and electric vehicles and may play an increasingly important role also in large-scale energy storage as our energy production systems are globally shifting towards variable renewable energy sources such as solar and wind power. For all these applications, electrolyte improvements are, even if not always recognized, in high demand due to both safety concerns and additional cost arising from their flammability and high vapor pressure.¹ In addition, the electrolytes are not especially thermally stable, primarily as the ubiquitous PF₆⁻ anion auto-decomposes into toxic compounds.² They are also not as electrochemically stable as needed at high voltages; today the aim of LIBs is set for *ca.* 5.0 V vs Li⁺/Li⁰.³

Unfortunately, the many requirements on LIB electrolytes means that their composition is hard to vary without impeding their functionality. Indeed, apart from the quite many different additives employed, the electrolyte composition has more or less remained unchanged since a few years after the commercialization of LIBs: 1 M LiPF₆ dissolved in a solvent mixture of a cyclic carbonate, often ethylene carbonate (EC), and a non-cyclic carbonate, most often dimethyl carbonate (DMC).⁴ While these electrolytes have a balanced set of properties, they have been optimized to the point where minor changes cannot substantially improve their safety and stability properties. Thus, any novel high energy density LIB chemistry likely requires a conceptually different electrolyte. In this respect, while solid electrolytes are attracting a lot of interest at present due to their potential to eliminate flammability and enable higher energy density,⁵ many problems remain to be solved for these to be practical; low ionic conductivity, structural integrity, electrolyte-electrode contact, etc. At present, liquid electrolytes is still the main-track in practice.

One emerging liquid electrolyte concept that potentially can improve safety and performance of LIB electrolytes is highly concentrated electrolytes (HCEs), a.k.a. super-concentrated or

solvent-in-salt electrolytes.^{6–8} HCEs are a class of electrolytes where the concentration of salt is comparable to the concentration of solvent in terms of molar ratio, resulting in *ca.* 3–5 M electrolytes. This change as compared to *ca.* 1 M traditional electrolytes, where the molar ratio typically is ≥ 10 , has profound implications on the local structure in the electrolyte, as there is not enough solvent present to fully solvate the Li⁺ ions. This also affects the electrochemical stability, as the local structure determines the vulnerability to oxidation/reduction, and thus determines both the size of the electrochemical stability window (ESW) as well as the electrolyte decomposition products,⁹ which in turn affects the ability to passivate the electrodes. Increasing the electrolyte salt concentration has been demonstrated to enable reversible cycling at both lower^{9–12} and higher^{13–15} potentials than the corresponding less concentrated electrolytes. First proposed for LIBs by McKinnon and Dahn as early as 1985,¹⁰ HCEs have gained much renewed interest in more recent years for both LIBs^{11,12,16–18} and lithium metal based batteries.^{19,20} HCEs can also be varied almost endlessly in composition,^{6,7} enabling their usage also for battery chemistries based on other cations than Li⁺, e.g. Na⁺ for sodium-ion batteries (SIBs).^{21–25}

The mechanism(s) of cation transport in HCEs has been subject of much discussion, but surprisingly limited computational investigation.^{26–28} The higher degree of ion-ion interaction^{9,29,30} means that the vehicular ion transport mechanism⁴ of traditional electrolytes, in which fully solvated cations migrate with their first solvation shell at a rate limited by the electrolyte viscosity, i.e. following a Stokes-Einstein limited behavior, should not at all be dominant, or perhaps not even possible. This hypothesis is supported by experimental findings of higher transport numbers for Li⁺ in HCEs as compared to traditional LIB electrolytes.^{20,31,32} Instead, ligand-exchange mediated mechanisms have been suggested by Okoshi et al.²⁸ and Seo et al. have argued that the ionicity, i.e. the degree of cation-anion coordination, as well as the solvent and anion residence times should be as important as viscosity in explaining HCE transport mechanisms.²⁷ Nilsson et al. have shown by a combination of experimental techniques that while species

^zE-mail: rasmus.andersson@chalmers.se; patrik.johansson@chalmers.se

diffusivity tends to increase with decreased viscosity, ionic conductivity depends more strongly on ionicity, and also seems to be more predictive of rate capability in electrochemical cells.³² From a computational point of view, Åvall et al. have found that increasing salt concentration leads to larger, more varied solvation shells with lower energy barriers, which in turn enables faster kinetics, and probably ion transport.^{22,23} Altogether it is very clear that a more direct molecular-level understanding of the ion transport mechanism (s) in HCEs is needed, and this presupposes knowledge of both the structure and the dynamics of such electrolytes.

While continuum models of ion transport, e.g. the family of models originating in the work of Newman and co-workers,^{33–35} have been very useful in understanding the overall interplay between cell components and the effects of physicochemical properties on performance, they cannot be used to gain understanding of structure or dynamics on the molecular level. Thermodynamic lattice models,³⁶ do have the potential to advance the fundamental understanding of HCEs, but they need to be supplemented with molecular level data to be accurately applied to specific electrolytes. Molecular dynamics (MD) simulations, on the other hand, is an indispensable tool for a better understanding of both structure and dynamics in liquids in general³⁷ as well as for LIB electrolytes.^{22,28,30,38–47} In general, MD simulations provide large amounts of detailed data for a specific system, or family of systems, that can be analyzed statistically to e.g. elucidate solvation structure and dynamics as well as ion transport properties and mechanisms. Given that accurate MD simulations are performed long enough to capture the relevant dynamics, statistical analysis of MD trajectories can be used either to predict macroscopic properties, or conversely explain their molecular level origins. For both LIB and SIB electrolytes, MD simulations have been used to elucidate the structure of the first solvation shell of the cation^{22,28,30,38–46} and ligand angle distributions,^{22,39,41,47} as well as ionic diffusivities.^{28,38,39,41,44–46}

These kinds of analyses for standard LIB/SIB electrolytes are straight-forward since the molecular structure is known *a priori*. However, the structure of the first solvation shell of the cation is less explanatory/useful when the cation is embedded in larger aggregates—as is arguably the case for all HCEs. Similarly, describing transport exclusively in terms of total ion diffusivity loses explanatory power when the transport is to a substantial extent mediated by changes in the local environments of the ions. When structures not known in detail and which furthermore change on time-scales relevant for transport processes determine the behavior, there is a need for more advanced post-analysis of MD simulation trajectories in order to elucidate the ion transport mechanism(s).

We here present a novel and general method for automatically detecting and characterizing the time-dependent structure, dynamics, and ion transport of HCEs (or in fact more or less any type of electrolyte), based on post-processing MD simulation trajectories. Our method is based on identifying bonds, including both covalent and coordination bonds, between atoms based on their dynamics, and subsequently classifying different local structures by their bond topology as subsets of the global bond graph. These topologies are finally characterized using statistical physics to evaluate their dynamical properties, e.g. mean lifetimes and contributions to Li⁺ ion diffusivity. The local bulk electrolyte processes we target here are essentially the same regardless of whether an external field is present or not, i.e. migration is approximated. This is a well-founded approximation as the fields created by an external cell potential would be several orders of magnitude weaker than the electrostatic interactions and activation energies/barriers controlling local ion transport events. Our method, while clearly a molecular level description, also starts to bridge the gap between molecular and macroscopic models, as urged for^{48,49}: by providing mechanistic understanding of the local structure and dynamical processes it can guide model design and clarify the realism of assumptions underlying macroscopic models.

We demonstrate our method by applying it to the well-studied HCE lithium bis(trifluoromethanesulfonyl)imide (LiTFSI) dissolved

in acetonitrile (ACN) at 1:2 molar ratio of salt:solvent. Brouillette et al.²⁹ and Seo et al.³⁰ have both studied the structure of this electrolyte by combining differential scanning calorimetry with Raman spectroscopy and found it to be amorphous at all temperatures. However, the overlapping Raman bands made a full spectral deconvolution impossible and hence limited the information on the ion-ion and ion-solvent interactions. Both studies found roughly half of the TFSI anions to be coordinated to Li⁺. In contrast, Yamada et al.,⁹ combining Raman spectroscopy and *ab initio* MD (AIMD), found almost all TFSI ions to be coordinated to Li⁺, giving rise to a liquid percolating network. Seo et al. also employed *ab initio* and density functional theory (DFT) calculations to determine solvation shell formation energies, as well as classical MD simulations, and found the TFSI anions to be predominantly but monodentately coordinated to the Li⁺ cations. In a follow-up study,²⁷ wherein they compared the ion transport properties of different electrolytes as function of salt concentrations, these did not clearly correlate negatively with the viscosity, strongly suggesting contributions from some kind of non-vehicular ion transport mechanism. They also evaluated the residence times of the anions and the solvent molecules in the first solvation shell of the Li⁺ cation based on MD simulation trajectories and these were typically on the order of hundreds of ps. Lundgren et al.³¹ later used the same HCE and by a combination of Newman style modelling and electrochemical characterization they found considerably higher cation transport numbers than for traditional LIB electrolytes.

In terms of increased electrochemical stability, Matsumoto et al.¹³ found the cathode Al current collector corrosion induced by conventionally concentrated LiTFSI based electrolytes to be suppressed at higher concentrations. They attributed this to preferential formation of passivating inorganic LiF on the Al surface, but this was questioned by McOwen et al.,¹⁵ suggesting that the high TFSI concentration together with a low concentration of “free” solvent allows the positively charged surface to be essentially covered by passivating anions. This is somewhat reminiscent to the Chazalviel theory of high salt concentration passivation.⁵⁰ On the anode side, Yamada et al.⁹ observed reversible Li⁺ intercalation into graphite, even without any solid electrolyte interphase (SEI) forming EC present in the electrolyte composition. They suggested the liquid percolating network to shift the LUMO from being ACN centered to be located on the TFSI anion due to the extensive coordination by Li⁺, enabling a stable SEI to be formed. Thus also the extended ESWs of HCEs originate in a different local structure and can thus also be better understood by appropriate models, even if both the quality of the SEI and the suppression of Al corrosion later, however, were found to be inadequate for cycling using relevant cell conditions.⁵¹

In what follows, we first describe our novel method for detecting, classifying and characterizing the local structures and dynamics in electrolytes. We then provide the computational details of the AIMD simulation that serves as input data for our analysis. We thereafter present and discuss our results in terms of structure and dynamics with a special emphasis on the Li⁺ ion transport.

Methods

Structure detection and dynamical characterization.—All chemical bonds, including also ion-ion and ion-solvent coordination bonds, in the AIMD simulation trajectory were identified using our recently developed software CHAMPION (Chalmers Atomic, Molecular, Polymeric & Ionic analysis toolkit), based on the dynamics of pairs of neighboring atoms. For a pair of atoms to be identified as bound, they need to oscillate about an equilibrium distance of each other over several vibrational cycles (Fig. 1, center). For coordination bonds, the times of formation and breakage were also identified where applicable. Subsequently, a time-dependent bond graph is constructed: an undirected colored graph where the nodes represent atoms and the edges represent bonds (Fig. 1, right).

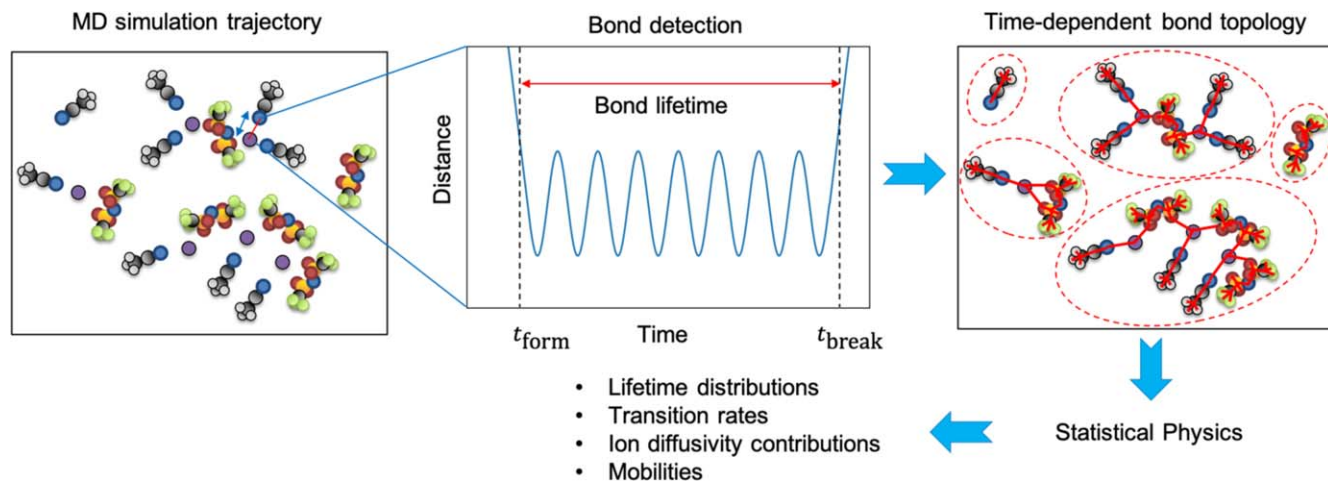


Figure 1. Schematic of our novel method. Element colors: purple: Li, red: O, blue: N, grey: C, white: H, yellow: S, green: F.

The global structure is characterized by the connected components of the time-dependent bond graph (dashed ellipses around components in Fig. 1). Local environments of ions and molecules are identified by the subgraphs consisting of all atoms and bonds up to a selected number of bonds away from a central atom, e.g. Li^+ . The distinct types of connected components and local environments are classified by their subgraph topology, with each topology characterized statistically by sampling:

- The probability of atoms of the considered element to be in each topology at any given time,
- Their lifetime distributions, estimated by fitting a stretched exponential function for the survival probability as a function of lifetime,
- Transition rates, and
- The contributions to diffusive transport.

While we here focus on the Li^+ cation, we also performed the same analysis for both TFSI and ACN (SI).

The total diffusivities of Li^+ , TFSI and ACN were determined using

$$D_X = \frac{1}{6} \left\langle \frac{d}{d\tau} \Delta \vec{r}^k(t, t + \tau)^2 \right\rangle_{k,t,\tau} \quad [1]$$

where $X \in \{\text{Li}^+, \text{TFSI}, \text{ACN}\}$ denotes the species and k enumerates exemplars of X , $\Delta \vec{r}^k(t, t + \tau)^2 = (\vec{r}^k(t + \tau) - \vec{r}^k(t))^2$ is the squared displacement of k between times t and $t + \tau$, and the average goes over all exemplars, all times between 0 and $T - \tau$ for a trajectory of length T , and τ goes between the diffusion onset time, defined as the interval beyond which the mean squared displacement (MSD) grows linearly as opposed to quadratically, and T .

To study transport mechanism(s) we decompose the total diffusivities of the ions and solvent into additive contributions from each different local environment topology and the transitions between them, corresponding to vehicular and non-vehicular transport mechanisms broadly construed, as moving either along with or relative to the local environment, e.g. the first solvation shell in the case of Li^+ . The diffusivities of local environments are in general impossible to assess from the data if their lifetimes are not significantly longer than the diffusion onset time. However, we are here considering not their own long-time transport but their contributions to that of the ions and the solvent. We start by decomposing the instantaneous velocity of exemplar k of species X into vehicular and non-vehicular contributions from local environment topologies and their transitions. We define

$$\vec{v}_{ii}^k(t) = \chi_i^k(t) \vec{v}_{\text{com}}^k(t) \quad [2]$$

and

$$\vec{v}_{ij}^k(t) = \xi_{ij}^k(t) (\vec{v}^k(t) - \vec{v}_{\text{com}}^k(t)) \quad [3]$$

as the diagonal and non-diagonal contributions to instantaneous velocity w.r.t. topologies, where $\chi_i^k(t)$ is an indicator function active when k has local environment topology i and $\vec{v}_{\text{com}}^k(t)$ is the center-of-mass velocity of the local environment, and $\xi_{ij}^k(t)$ is an indicator function active between the midpoints of the lifetimes of two consecutive local environments of topologies i and j where j transitions to i . By this construction, $\vec{v}_{ii}^k(t)$ and $\vec{v}_{ij}^k(t)$ add up to the total velocity:

$$\vec{v}^k(t) = \sum_i \vec{v}_{ii}^k(t) + \sum_{i \neq j} \vec{v}_{ij}^k(t) = \sum_{i,j} \vec{v}_{ij}^k(t) \quad [4]$$

where one diagonal and one non-diagonal term of the right-hand side is non-zero at each value of t .

The switching of $\xi_{ij}^k(t)$ at midpoints might seem arbitrary, but note that most of the non-vehicular contributions to squared displacement are expected to occur near transitions between environments, as the effects of e.g. rotational and vibrational motion within a topology tends to cancel out over time, whereas leading up to or following a structural rearrangement they may well contribute meaningfully to transport if they occur frequently, consider e.g. ion hopping mechanisms. Switching at midpoints minimizes the effects of the switching on assignment as the midpoints are the furthest removed from the transitions.

By this velocity decomposition, the contribution to X diffusivity due to transition from j to i (or due to vehicular motion of topology i if $i = j$) is given by

$$D_{X,ij}^* = \frac{1}{3} \langle \Delta \vec{r}^k(t, t + \tau) \cdot \vec{v}_{ij}^k(t + \tau) \rangle_{k,t,\tau} \quad [5]$$

which is arrived at by expanding one of the terms in the square in Eq. 1 and carrying out the differentiation w.r.t. τ .

Since $D_{X,ij}^*$ is an additive contribution to the total diffusivity, it is proportional to P_j , the probability of X having topology j . Dividing by P_j gives a measure of effective diffusivity, which allows mechanisms to be compared. For diagonal, i.e. vehicular, mechanisms, $D_{X,ii}^{\text{eff}} = D_{X,ii}^*/P_{X,i}$ is a measure of how mobile the topology is in the system. For non-diagonal, i.e. non-vehicular, mechanisms, diffusivity contributions can be written as $D_{X,ij}^* = P_{X,j} Q_{X,ij} d_{X,ij}^2$ where $Q_{X,ij}$ is the (left-stochastic) transition rate matrix for

topologies of X and $d_{X,ij}$ is an effective distance traveled due to the transition, defined by this relation. Since $Q_{X,ij}$ can be measured independently, $d_{X,ij}$ can be determined using $d_{X,ij}^* = D_{X,ij}^* / P_{X,j} Q_{X,ij}$. Non-vehicular transport mechanisms can thus be studied in terms of how the composition of local environments affect $Q_{X,ij}$ and $d_{X,ij}$.

From a local structure point-of-view, in addition to the detailed analysis in terms of first solvation shell composition, we also analyzed, in a more coarse-grained fashion, the Li^+ solvation numbers (SNs): the total number of ligands, and coordination numbers (CNs): the total number of coordination bonds, i.e. taking into account the possibility of e.g. bidentate coordination. Similarly, but for the dynamics, we extracted the transport number t^+ , i.e. the fraction of the Li^+ ion diffusivity to the total ionic diffusivity ($D_{\text{Li}^+} / (D_{\text{Li}^+} + D_{\text{TFSI}})$), from the AIMD simulation trajectory.

AIMD simulations.—An AIMD simulation within the NVT ensemble was performed at 293 K using a Nosé-Hoover thermostat with $\omega_{\text{ions}} = 2250 \text{ cm}^{-1}$ and $\omega_{\text{electrons}} = 4500 \text{ cm}^{-1}$ using the Car-Parrinello MD (CPMD)⁵² software and the Perdew-Burke-Ernzerhof (PBE)⁵³ functional. A system of 20 formula units (684 atoms in total) with a density of 1.48 g cm^{-3} ⁵⁴ was simulated in a cubic periodic box with side 21.57 \AA using a fixed time step of 0.1 fs for 6.33 ps, after first having equilibrated for 1.0 ps. The time needed for equilibration was found by considering the decay of the sum of pointwise squared errors of all partial radial distribution functions (RDFs) compared with their time average (Fig. S1 is available online at stacks.iop.org/JES/167/140537/mmedia). This deviation rapidly decreased for the first 0.7 ps, followed by fluctuations about a low average value $< 10\%$ of the original deviation, with no observable trend towards further decrease. During the equilibration time, each ion and molecule settles into its free energy minimum with regards to its nearest neighbors. Based on this, the equilibration time was conservatively set to 1.0 ps. While we cannot exclude the possibility of further

equilibration past the timescale of the simulation, the lack of a trend past 0.7 ps indicates any such processes to be orders of magnitude slower than the timescale of the simulation, and hence unreachable by AIMD simulations. To the extent that large-scale structural reorganization would be required to reach the global free energy minimum structure, we may expect our results to be somewhat biased towards entropy maximization rather than energy minimization, and consequently towards more rapid dynamics because of lower energy barriers to (de)complexation. While this bias may affect the relative proportion of the different structural species, and the absolute time-scale of dynamics and ion transport, it should not to first order affect the relative trends for the physicochemical properties among the structures as functions of their composition. The initial geometry was generated by randomizing and relaxing the positions and orientations of ions and molecules, by a conjugate gradient descent method w.r.t. a cost function designed to avoid overlap of atoms. The TFSI ions were initialized to 50% cis and 50% trans conformations, and pre-optimized using the Gaussian 16 software⁵⁵ at the M06-2X/6-311 + G(d, p) level of theory.⁵⁶

Results and Discussion

We first describe the distribution of coordination bonds for Li^+ and TFSI ions and the global electrolyte structure this gives rise to, before giving a more detailed description of the distinct Li^+ first solvation shell topologies and their solvation and ion coordination dynamics. We then move on to the transport properties, assessing and comparing the vehicular and non-vehicular contributions to diffusive transport of cations, anions and solvent. From this we propose an overall qualitative view of the Li^+ ion dynamics and transport mechanism, which we then study more closely. Finally, we present in rank order the most important contributions to the ion transport in terms of Li^+ CNs and transitions between them and

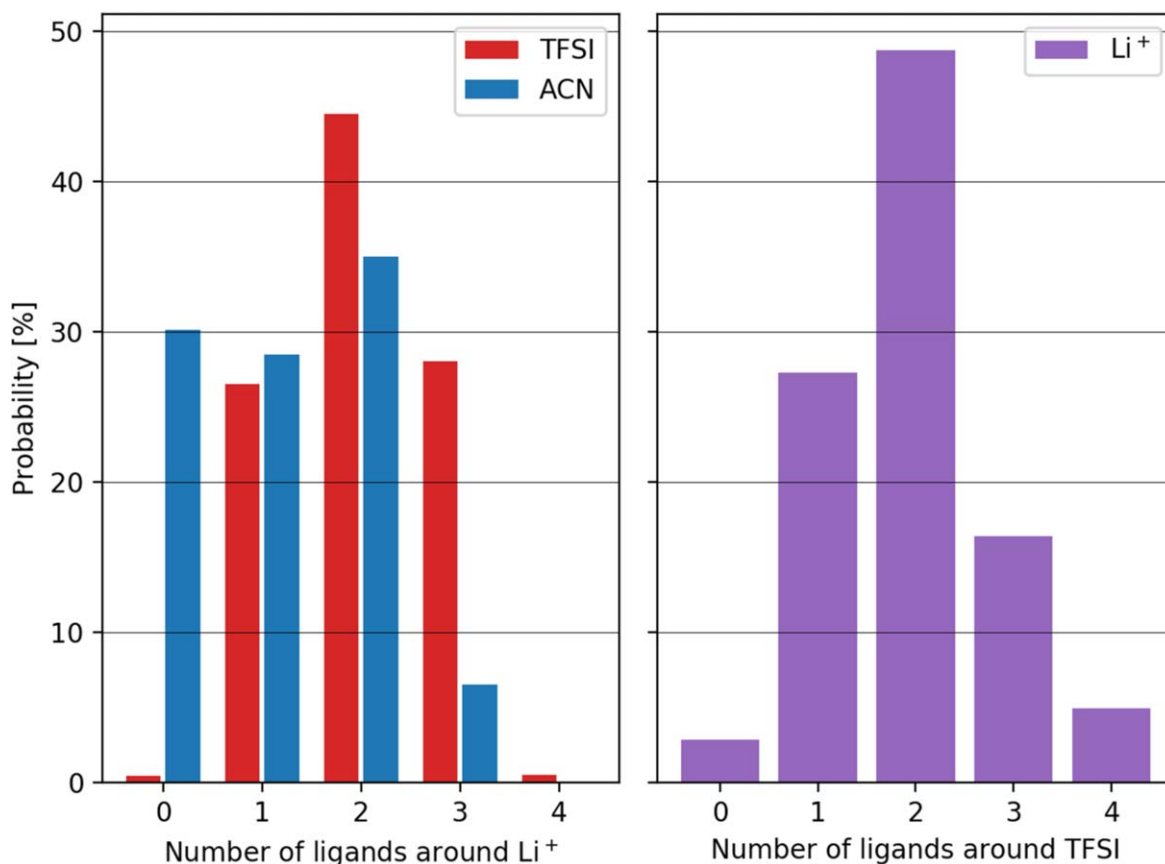


Figure 2. Distribution of (a) TFSI ions and ACN molecules coordinating to Li^+ and (b) Li^+ ions coordinating to TFSI.

analyze correlations between solvation shell composition and Li^+ diffusivity.

Electrolyte structure.—First of all, we consider the distribution of ligands around the Li^+ ions and the distribution of Li^+ ions coordinating the TFSI ions. The Li^+ ions on average coordinate with 2.0 TFSI ions and 1.2 ACN molecules, thus giving a total average SN of 3.2 (Fig. 2a). While Seo et al. found a similar partial ACN SN (1.0) from their Raman data,³⁰ their classical MD data resulted in SNs of 2.42 and 1.45, for TFSI and ACN, respectively. While much higher in absolute numbers, likely due to using different cut-off distances, our and their ratios of TFSI/ACN are however almost identical, both ≈ 1.67 —hence similarly composed local structure around the Li^+ ions. Due to the possibility of bidentate coordination by the TFSI anions, the average Li^+ CN is slightly greater than the SN, 3.5, and furthermore CN=4, typical for Li^+ in organic solvents,⁴ holds for slightly more than half of the Li^+ ions—to be explored together with the topologies and transitions further below (Fig. 7a).

Looking at the distribution of ligands, all but a very negligible fraction (0.4%) of the Li^+ ions coordinate to at least one TFSI ion: roughly half of them to two anions, and a quarter of them each to one and three anions, respectively. While a similarly very tiny fraction (0.5%) coordinate to four different TFSI ions, there are thus very few “free” Li^+ ions present at any stage—almost all are to some extent subject to ion-ion interactions. The first solvation shells are completed by ACN molecules for some Li^+ ions, and these are more or less evenly distributed between zero and two ligands, *ca.* 30% each, with a small fraction (6.5%) solvated by three ACN molecules. From the perspective of the TFSI anion, the distribution is centered at 1.9 coordinating Li^+ ions on average with a clear majority of TFSI anions coordinating to more than one Li^+ ion, roughly a quarter with one and a negligible fraction is “free” (Fig. 2b).

The high degree of ion-ion interaction and coordination, *i.e.* each ion coordinates *ca.* two ions of the opposite charge, gives rise to a percolating network structure of alternating cations and anions in which *ca.* 90% of the ions participate on average (Fig. 3). The remaining *ca.* 10% exist in ion-pairs and finite clusters; most of the latter consist of one or two ions of each kind and none contain more than ten ions (Fig. 4). Notably, about three quarters of the finite clusters are charge neutral. While this overall shows a significantly higher degree of ion-ion interaction and coordination than reported by both Brouillette et al.²⁹ and Seo et al.,³⁰ it is in good agreement with Yamada et al.⁹ The discrepancies may, at least in part, be

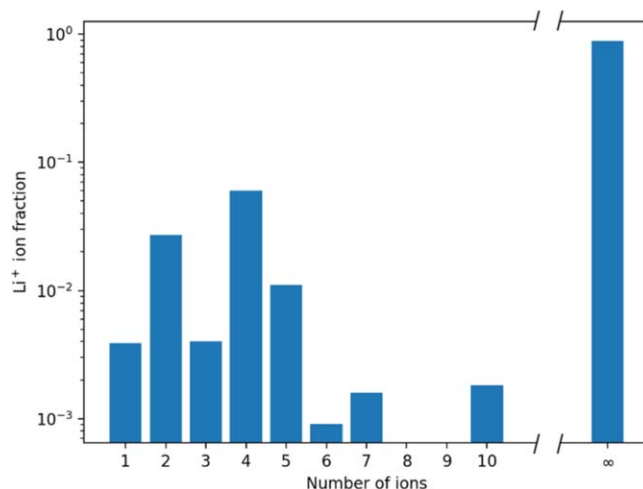


Figure 4. Distribution of the total number of ions per cluster (and the network).

explained by the reported difficulties encountered when trying to distinguish contact ion-pairs (CIPs) from solvent-separated ion-pairs (SSIPs) using Raman data.^{27,30}

Turning to the percolating network structure it can be understood in terms of a branching process. A Markovian process starting from a single Li^+ ion and branching out according to the probability distribution of coordinating TFSI ions would in the first step equate the distribution shown in Fig. 2. A continued branching from each of the TFSI ions will give them a probability distribution of additional Li^+ ion ligands with the condition of having at least one, at an expectation value of 0.989. In the next step, each Li^+ ion coordinates to similarly conditioned TFSI ions with an expectation value of 1.025. Due to the Markovian assumption, pairs of consecutive branching steps can be combined into a single one with a branching factor of $0.989 \cdot 1.025 = 1.014$, which then corresponds to the expectation value for the other Li^+ ions sharing a TFSI ion with a given Li^+ ion. Except for the first step, this is a Galton-Watson process, for which a well-known result is that there is a finite probability of indefinite survival, corresponding to forming a percolating network, when the branching factor is greater than 1. Our electrolyte is thus poised just above the percolation threshold;

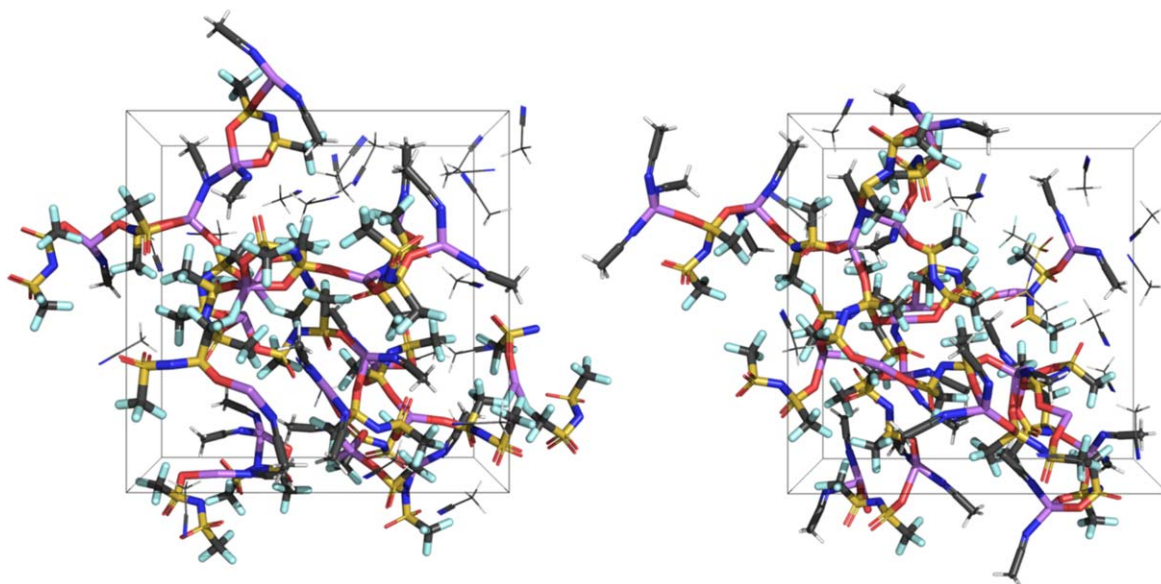


Figure 3. Snapshots of the periodic simulation cell, highlighting the alternating ion network. While the network binds with its images in neighboring cells, here only one copy of each atom is included. Element colors: purple: Li, red: O, blue: N, grey: C, white: H, yellow: S, green: F.

and most likely a modest decrease in salt concentration would lead to a non-percolating structure, and hence quite different properties. The ACN molecules have little effect on the network structure apart from competitively coordinating Li^+ ions; they are roughly evenly distributed between non-coordinating and coordinating a single Li^+ ion, with very few (<2%) being shared between two Li^+ ions (Fig. S5).

We further analyzed the electrolyte local structure in more detail by considering all Li^+ first solvation shells; the fifteen most common topologies are shown in Fig. 5, while their probabilities, relative contributions to the Li^+ diffusivity, effective diffusivity and mean lifetimes are presented in Table I. In the latter all values are presented as averages with an uncertainty (one standard deviation) also taking into account the statistical inefficiency of the sampling. The exact numbers and ordering should in general be interpreted with some caution due to the possible bias towards entropically favored structures and rapid dynamics discussed above, as well as the risk that the trajectory does not fully sample the ensemble.

The most common first solvation shell topology, accounting for roughly a fifth of the Li^+ first solvation shells, consists of two TFSI ions and two ACN molecules, with both TFSI ions coordinating monodentately. The next two most common topologies consist of three TFSI ions and three TFSI ions and one ACN molecule, respectively, clearly illustrating the preferential TFSI coordination. Most of the coordination is monodentate by the sulfonyl oxygen atoms, in agreement with Seo et al.,³⁰ but similar bidentate coordination is also relatively common, while bidentate coordination by one oxygen atom and one nitrogen atom occurs less frequently, as does coordination only to the nitrogen atom or to a fluorine atom. The latter are also considerably shorter-lived. ACN always coordinates monodentately to Li^+ , as expected.

The Li^+ first solvation shells have quite rapid solvation dynamics, with lifetimes mostly ranging between 0.2–0.9 ps. The $\text{Li}(\text{TFSI})(\text{ACN})_3$ topology ($i = 4$) is an outlier, with a mean lifetime of >2 ps, but note that the uncertainty is very large. For individual species, the residence time of TFSI is on average *ca.* 6 ps and that of ACN is only slightly shorter (Table I). While these residence times are orders of magnitude shorter than those of Seo et al.,²⁷ we attribute these differences in part to their very inclusive choice of cut-off distance, and in part to the possible bias towards rapid

dynamics discussed above. Our results are, however, of the same order of magnitude as reported elsewhere for other HCEs.²³

The Li^+ first solvation shell lifetime exhibits a moderate correlation ($r = 0.43$) with the total CN, reflecting the stability of CNs 3 and 4 (higher CNs are rarely encountered, Fig. 7a). Most of the variance can be explained by the variation in partial ACN CN ($r = 0.38$), reflecting its greater variance compared to the partial TFSI CN (Fig. 2a).

Transport properties and mechanisms.—An overall picture of the ionic and molecular transport is arrived at by considering the total diffusivities of the respective species, and the degree to which they are vehicular vs non-vehicular in nature (Fig. 6). The vehicular diffusivities of Li^+ and TFSI are quite similar, which is expected since most ions are part of the percolating network, and three quarters of the finite clusters have equal numbers of cations and anions (Fig. S3). The slightly higher vehicular diffusivity of TFSI is likely due to the non-negligible fraction of “free” TFSI ions, *ca.* 5% (Fig. 2b), being more mobile than the Li^+ ions (Tables I, SI), though the difference is within the margin of error—a comparable phenomenon as observed in ionic liquid based electrolytes by e.g. IR, Raman and NMR spectroscopies.^{57,58} However, the large fraction of non-vehicular transport, from fast solvation dynamics and high degree of ion association, affects Li^+ and TFSI differently. The overall effect is that Li^+ has a higher diffusivity and $t^+ = 0.63$, in reasonable agreement with Lundgren et al. (*ca.* 0.72).³¹ In stark contrast, but as expected, ACN has a higher diffusivity that is almost exclusively due to vehicular transport, reflecting that a substantial fraction of the ACN molecules are free and much more mobile than the percolating network.

By observing animations of the trajectory, we can start to also qualitatively understand the reasons why the network structure facilitates a higher non-vehicular diffusivity for Li^+ . It is clear that the TFSI ions form the backbone of the percolating network structure, with the Li^+ ions contributing with dynamic cross-links, so as to create a structure whose geometry and segmental motion are largely determined by the nature of the TFSI anions. The hard, in a HSAB sense,⁵⁹ Li^+ ion coordinates strongly to all its ligands and oscillates with large amplitude inside its solvation cage. Due to the large internal flexibility of the TFSI anion⁶⁰ the network structure

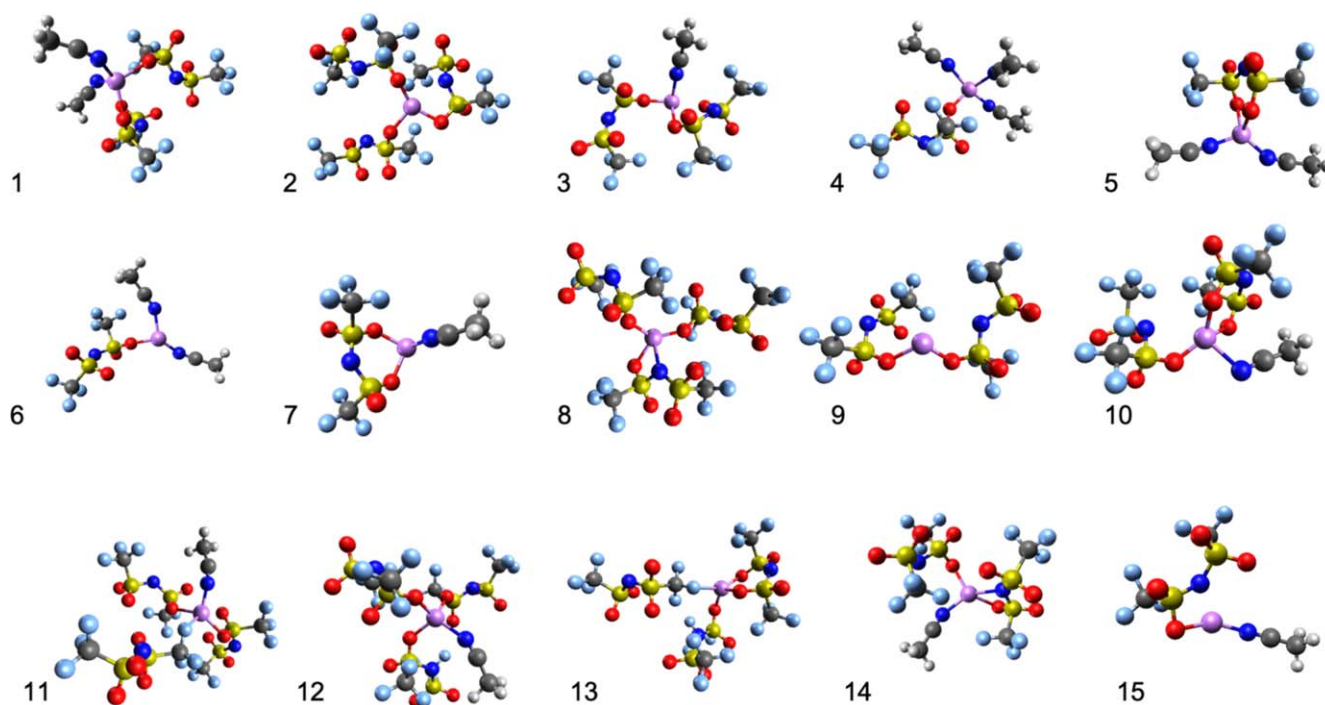
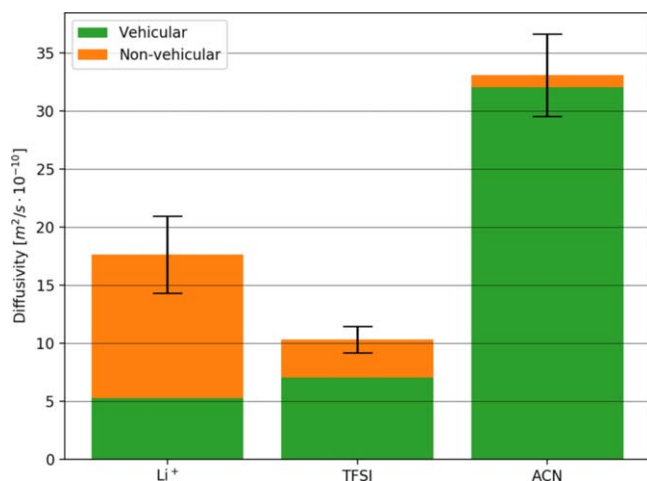


Figure 5. The most common topologies around Li^+ in order of probability. Element colors: purple: Li, red: O, blue: N, grey: C, white: H, yellow: S, green: F.

Table I. Properties of the most common topologies around Li^+ .

i	Topology	Probability	$D_{\text{Li}^+,ii}^*/D_{\text{Li}^+}$	$D_{\text{Li}^+,ii}^{\text{eff}} [10^{-10}\text{m}^2/\text{s}]$	Lifetime [ps]
1	$[\text{Li}(\text{TFSI})_2(\text{ACN})_2]^-$	$20.8 \pm 0.6\%$	$5.9 \pm 0.4\%$	5.00 ± 0.16	0.82 ± 0.09
2	$[\text{Li}(\text{TFSI})_3]^{2-}$	$10.9 \pm 0.5\%$	$2.2 \pm 0.2\%$	3.56 ± 0.17	0.44 ± 0.06
3	$[\text{Li}(\text{TFSI})_2(\text{ACN})]^-$	$8.3 \pm 0.3\%$	$1.7 \pm 0.1\%$	3.53 ± 0.14	0.28 ± 0.07
4	$\text{Li}(\text{TFSI})(\text{ACN})_3$	$6.0 \pm 0.4\%$	$1.7 \pm 0.2\%$	4.88 ± 0.34	2.18 ± 0.56
5	$\text{Li}(\text{TFSI}_{\text{OO}})(\text{ACN})_2$	$5.9 \pm 0.4\%$	$3.0 \pm 0.2\%$	8.85 ± 0.62	0.87 ± 0.23
6	$\text{Li}(\text{TFSI})(\text{ACN})_2$	$5.2 \pm 0.2\%$	$4.2 \pm 0.3\%$	14.18 ± 0.60	0.18 ± 0.04
7	$\text{Li}(\text{TFSI}_{\text{OO}})(\text{ACN})$	$4.9 \pm 0.4\%$	$0.4 \pm 0.1\%$	1.48 ± 0.14	0.49 ± 0.04
8	$[\text{Li}(\text{TFSI})_2(\text{TFSI}_{\text{ON}})]^{2-}$	$4.6 \pm 0.3\%$	$0.8 \pm 0.1\%$	3.18 ± 0.22	0.59 ± 0.14
9	$[\text{LiTFSI}_2]^-$	$4.2 \pm 0.3\%$	$0.5 \pm 0.1\%$	2.06 ± 0.17	0.23 ± 0.05
10	$[\text{Li}(\text{TFSI})(\text{TFSI}_{\text{OO}})(\text{ACN})]^-$	$3.5 \pm 0.3\%$	$0.2 \pm 0.04\%$	0.76 ± 0.08	0.34 ± 0.06
11	$[\text{Li}(\text{TFSI})_2(\text{TFSI}_{\text{F}})(\text{ACN})]^{2-}$	$2.2 \pm 0.2\%$	$1.2 \pm 0.1\%$	9.30 ± 17.2	0.19 ± 0.03
12	$[\text{Li}(\text{TFSI})_3(\text{ACN})]^{2-}$	$2.1 \pm 0.2\%$	$0.7 \pm 0.02\%$	5.54 ± 0.56	$0.74 \pm 2\text{e-}4$
13	$[\text{Li}(\text{TFSI})(\text{TFSI}_{\text{OO}})(\text{TFSI}_{\text{F}})]^{2-}$	$2.0 \pm 0.2\%$	$0.04 \pm 0.09\%$	0.35 ± 0.19	$0.33 \pm 1\text{e-}8$
14	$[\text{Li}(\text{TFSI})(\text{TFSI}_{\text{ON}})(\text{ACN})]^-$	$1.7 \pm 0.2\%$	$0.04 \pm 0.07\%$	0.42 ± 0.18	0.23 ± 0.03
15	$\text{Li}(\text{TFSI})(\text{ACN})$	$1.6 \pm 0.1\%$	$0.8 \pm 0.2\%$	9.04 ± 0.74	$0.34 \pm 8\text{e-}9$

**Figure 6.** Diffusivities of electrolyte species partitioned into vehicular and non-vehicular contributions. The error bars denote 95% confidence intervals for the total diffusivities.

continually deforms, leading to some drift in the absolute position of the Li^+ ion. This contributes to the vehicular transport that affects Li^+ and TFSI equally and occasionally facilitates the formation of new coordination bonds. Sometimes, the electrostatic environment of a Li^+ coordination bond weakens it enough for a ligand to drift away without giving rise to a strong recoil and thereby the topology, CN and/or SN can be altered, additionally by new ligand(s): nearby TFSI anions and/or free ACN. A new strong Li^+ first solvation shell is formed along with a new equilibrium position. When the new ligand is a TFSI ion, most already coordinated to one or more Li^+ ions in the percolating network and thus immobilized, the event is more pronounced. The large and flexible TFSI, which usually is constrained by coordination bonds, rotates and deforms to bring the sulfonyl oxygen atoms closer to Li^+ , which on the other hand, only has a single translative degree of freedom. Overall, all this sums up as a structural diffusion event. This mechanism is facilitated by the large number and angular diversity of possible coordination sites of the TFSI anion (due to its highly delocalized negative charge and extensive conjugation), and furthermore its internal flexibility enables new coordination bonds to form frequently. This is

supported by Åvall et al. ^{22,23}, showing that a higher CN variance is directly associated with faster ligand exchange.

We next consider the distribution of Li^+ CNs, as well as the transitions between them, both the rates and the distances moved (Fig. 7). More than half of the Li^+ ions have CN = 4, a third has CN = 3, and other CNs are much less prevalent, consistent with the former being more stable in terms of less negative transition rates along the diagonal. For the non-diagonal transition rates, there is a clear bias of probability flux towards the most stable CNs 3 and 4 compared to the fluxes from each CN in the other direction. The transition rates towards CNs 3 and 4 also increase with the distance from the most stable CNs.

Turning instead to the contributions to Li^+ diffusivity, over 80% of the transport is accounted for by the vehicular transport with CNs 3 and 4, as well as the structural transport due to the transitions between them, with most of the rest being due to transitions between CNs 3 and 2 (Fig. 8). This can be understood by considering the individual factors giving rise to $D_{\text{Li}^+,ij}$ (Fig. 7). Recalling that $D_{X,ij}^* = P_{X,j} Q_{X,ij} d_{X,ij}^2$ explains why CN 4 makes a large contribution, due to its high probability and the same applies to CN 3, but to a lesser extent. This is the main reason why both vehicular and non-vehicular transport of CNs 3 and 4 dominate over other Li^+ ion transport mechanisms. In addition, the transitions between these CNs are also connected to the largest distances moved (Fig. 7c), though this effect is less pronounced.

Finally, we assess the ion transport mechanisms in more detail by considering them in terms of the full structure of the first Li^+ solvation shell. Starting with an overview, the 13 most important transport events/mechanisms (having contributions >2% to the total) are ranked by their contribution to the Li^+ diffusivity (Fig. 9). Although these in total account for less than one-third of all Li^+ transport, they serve to illustrate some typical events/mechanisms and underscore the diversity of complex electrolytes. There are representatives of both vehicular and structural transport, and among the structural both exchanges of TFSI ions and ACN molecules as well as changes in the TFSI coordination.

Looking more closely at the vehicular transport mechanisms, Table I, we find a positive correlation coefficient $r = 0.36$ between the effective diffusivity $D_{\text{Li}^+,ij}^{\text{eff}}$ and the number of ACN molecules in the first Li^+ solvation shell, and a negative correlation coefficient $r = -0.42$ between $D_{\text{Li}^+,ij}^{\text{eff}}$ and the number of TFSI ions. Since these correlations almost cancel out, there is no strong correlation between effective diffusivity and total SN. From this we hypothesize that the

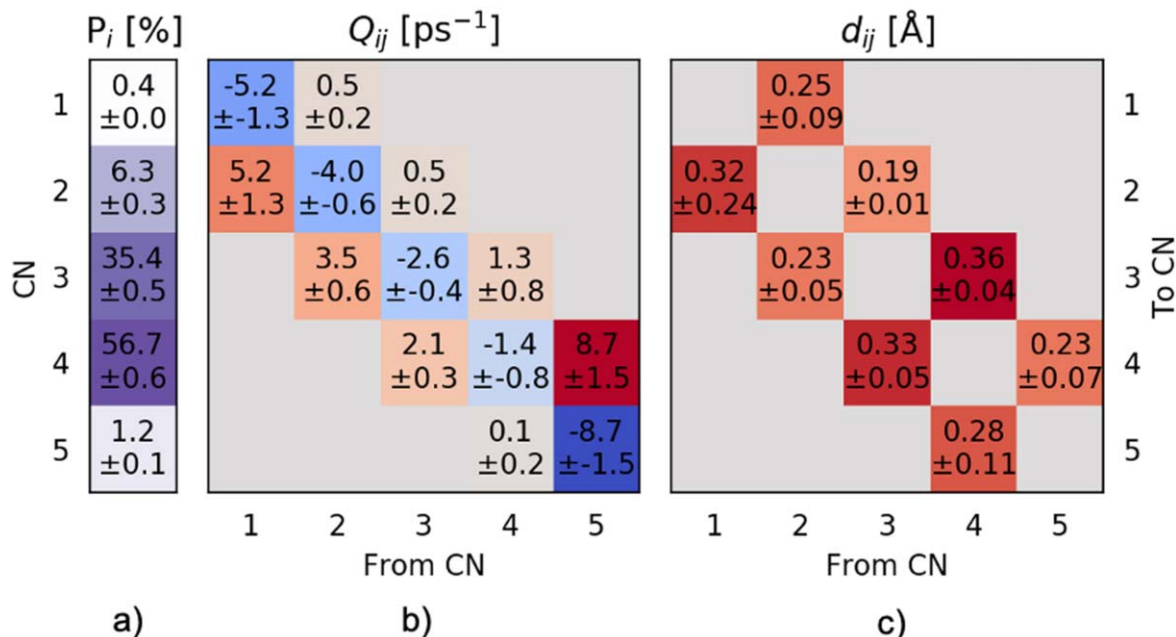


Figure 7. (a) Probability distribution, (b) transition rate and (c) distance matrices for Li^+ CN transitions.

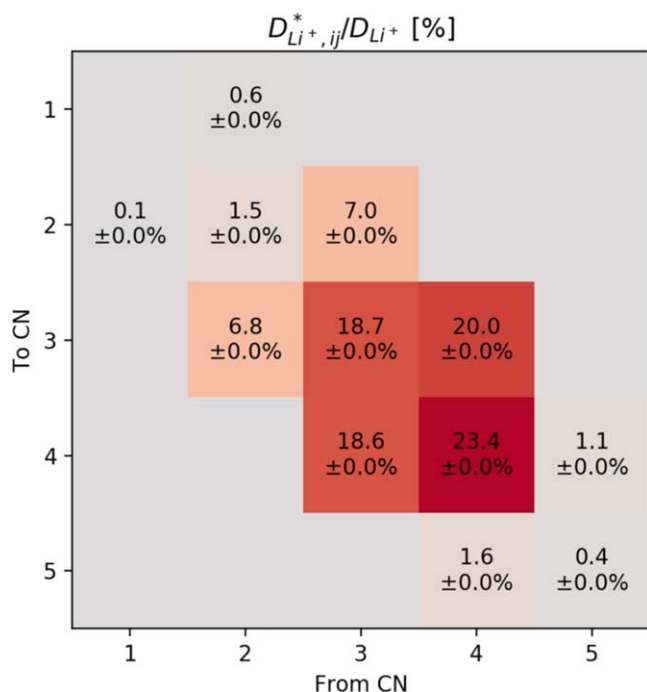


Figure 8. Relative diffusivity contributions of Li^+ CNs and transitions.

negative correlation is due to the TFSI immobilization in the percolating network structure, whereas the ACN blocks TFSI coordination. Furthermore, looking at the animated trajectory, the coordinated ACN tends to slightly change its orientation as a response to external steric hindrance during vehicular diffusion, thus limiting the slowing down else affecting all of the Li^+ first solvation shell.

For the non-vehicular mechanisms, there is a strong positive correlation ($r = 0.85$) between the effective diffusivity of a mechanism and the signed change in total SN, suggesting mostly associatively driven ion transport, consistent with our qualitative view above. Overall the most important mechanisms are

predominantly associative (six), while only two are dissociative (Table II, Fig. 9).

Conclusions

We found that our model HCE forms a flexible percolating network structure of alternating cations and anions including most of the ions, in which the Li^+ ions are partially solvated by ACN, but preferentially coordinate to the TFSI anions. The nature of the TFSI anion largely determines the overall structure and flexibility of the network, why these properties may change drastically for e.g. an HCE based on LiPF_6 . In light of the Galton-Watson theory for branched processes, our model system is just above the percolation threshold and thus slightly lowering the salt concentration would likely suffice to radically alter the global electrolyte structure and in turn the ion transport mechanism(s).

The network structure itself makes the vehicular Li^+ transport slow, but as very local fluctuations cause coordination bonds to occasionally break, this enables Li^+ ions to re-coordinate to e.g. a nearby TFSI ion, which while being largely immobilized in the network can rotate and deform. This way the network structure promotes diffusive transport of Li^+ to a much larger extent than for TFSI, leading to an observable increase in the Li^+ transport number—a common feature of HCEs that we thus here can address at the molecular level.

Based on this understanding, to maximize the Li^+ transport number, an HCE should be composed of large and flexible anions, such as TFSI, with many angularly distributed available coordination sites and in addition solvent molecules with similar ion-ion and ion-solvent interaction strengths with Li^+ to enable frequent ligand exchange. However, it is far from obvious how to improve these features beyond the TFSI anion—as its internal flexibility, negative charge delocalization⁶⁰ and versatile coordination geometry are all truly outstanding.

In a real operating battery, with electric fields and concentration gradients, the situation might differ somewhat. While these simulations and analysis do not account directly for migration, as in a true battery cell, the local events determining the ion transport in the bulk of the electrolyte are essentially the very same—but without a directional bias. Likewise, the situation at the two electrolyte/electrode interfaces/interphases likely differs from what we here can conclude from our bulk HCE steady-state AIMD simulations.

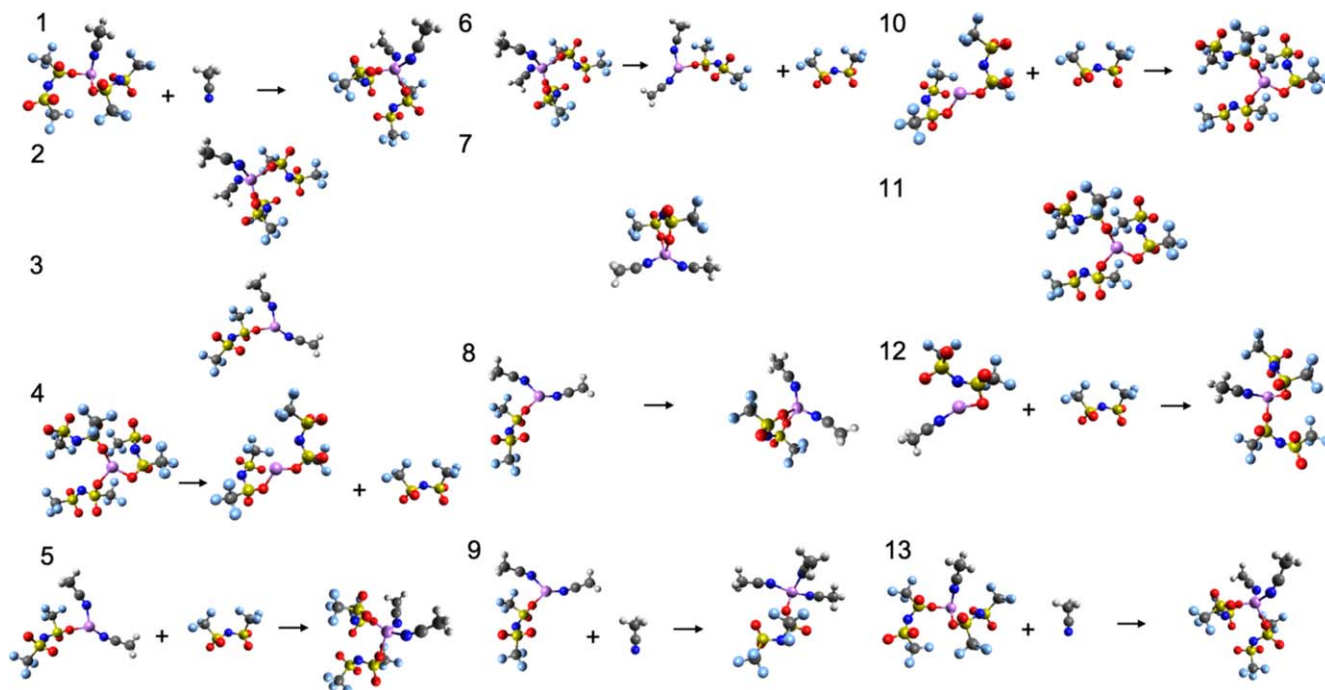


Figure 9. Most important Li + transport events/mechanisms in rank order. Element colors: purple: Li, red: O, blue: N, grey: C, white: H, yellow: S, green: F.

Table II. Properties of the most common transitions between local environments of Li⁺.

ID	j	i	Description	$D_{Li^+,ij}^*/D_{Li^+}$	Q_{ij} [ps ⁻¹]	d_{ij} [Å]
1	3	1	[Li(TFSI) ₂ (ACN)] ⁻ + ACN → [Li(TFSI) ₂ (ACN) ₂] ⁻	5.9 ± 0.6%	1.44 ± 0.55	0.47 ± 0.10
2	2	9	[Li(TFSI) ₃] ²⁻ → [LiTFSI ₂] ⁻ + TFSI ⁻	3.8 ± 0.7%	0.63 ± 0.16	0.23 ± 0.11
3	6	1	Li(TFSI)(ACN) ₂ + TFSI ⁻ → [Li(TFSI) ₂ (ACN) ₂] ⁻	3.7 ± 0.5%	3.12 ± 0.90	0.34 ± 0.06
4	1	6	[Li(TFSI) ₂ (ACN) ₂] ⁻ → Li(TFSI)(ACN) ₂ + TFSI ⁻	3.3 ± 0.6%	0.39 ± 0.08	0.54 ± 0.09
5	6	5	Li(TFSI)(ACN) ₂ → Li(TFSI _{OO})(ACN) ₂	2.6 ± 0.6%	0.89 ± 0.48	0.51 ± 0.21
6	6	4	Li(TFSI)(ACN) ₂ + ACN → Li(TFSI)(ACN) ₃	2.6 ± 0.5%	0.89 ± 0.48	0.51 ± 0.20
7	9	2	[LiTFSI ₂] ⁻ + TFSI ⁻ → [Li(TFSI) ₃] ²⁻	2.2 ± 0.7%	2.29 ± 0.71	0.27 ± 0.09
8	15	3	Li(TFSI)(ACN) + TFSI ⁻ → [Li(TFSI) ₂ (ACN)] ⁻	2.1 ± 1.6%	2.30 ± 0.29	0.37 ± 0.17
9	1	3	[Li(TFSI) ₂ (ACN) ₂] ⁻ → [Li(TFSI) ₂ (ACN)] ⁻ + ACN	1.9 ± 0.5%	0.39 ± 0.08	0.38 ± 0.07

Finally, the system size and trajectory length simulated are both too limited to ascertain the global structure and detailed statistics to be representative of the real bulk system, and larger and longer time-scale simulations would clearly be beneficial. Nevertheless, based on the fast dynamics of the first solvation shell (Table I), and the observed rapid equilibration of partial RDFs (Fig. S1), we are confident that the local structure and dynamics presented here are strongly indicative of the real system structure and dynamics.

In summary, our approach to understanding complex electrolytes, such as HCEs, by automatically detecting dynamic bonds and characterizing the structure and dynamics in terms of bond graph topology and statistical physics is a promising way forward towards rational design of electrolytes. The analysis method that we present here could also rather easily be extended to cover both longer simulation times and cover wider length-scales, to study global ion transport phenomena with better statistics. The most straightforward approach would be to replace our AIMD with classical MD. Another route would be to coarse-grain the electrolyte and apply simulation methods targeting the mesoscale such as kinetic Monte-Carlo.⁶¹ Indeed, our method should be well suited as one of the bottom layers in a comprehensive multi-scale approach for modelling electrochemical cells. We also expect that the methodology should generalize well to both similar application areas and other types of materials.

Acknowledgments

The research presented has received funding through the HELIS project (European Union's Horizon 2020 research and innovation program under Grant Agreement No. 666221) and the Swedish Energy Agency grants (#P43525-1 and #P39909-1). P. J. would also like to acknowledge several of Chalmers Areas of Advance: Materials Science, Energy, and Transport, for continuous support, and specifically the Theory and Modelling scheme of Advanced User Support to R.A. A.A.F. acknowledges the Institut Universitaire de France for the support.

ORCID

Rasmus Andersson <https://orcid.org/0000-0001-9359-1994>
 Patrik Johansson <https://orcid.org/0000-0002-9907-117X>

References

1. J. B. Goodenough and Y. Kim, *Chem. Mater.*, **22**, 587 (2010).
2. A. Hammami, N. Raymond, and M. Armand, *Nature*, **424**, 635 (2003).
3. V. Etacheri, R. Marom, R. Elazari, G. Salitra, and D. Aurbach, *Energy & Environmental Science*, **4**, 3243 (2011).
4. K. Xu, *Chem. Rev.*, **114**, 11503 (2014).
5. A. Manthiram, X. Yu, and S. Wang, *Nature Reviews Materials*, **2**, 1 (2017).
6. Y. Yamada and A. Yamada, *J. Electrochem. Soc.*, **162**, A2406 (2015).
7. Y. Yamada, J. Wang, S. Ko, E. Watanabe, and A. Yamada, *Nat. Energy*, **4**, 269 (2019).

8. O. Borodin, J. Self, K. A. Persson, C. Wang, and K. Xu, *Joule*, **4**, 69 (2020).
9. Y. Yamada, K. Furukawa, K. Sodeyama, K. Kikuchi, M. Yaegashi, Y. Tateyama, and A. Yamada, *JACS*, **136**, 5039 (2014).
10. W. R. McKinnon and J. R. Dahn, *J. Electrochem. Soc.*, **132**, 364 (1985).
11. S.-K. Jeong, M. Inaba, Y. Iriyama, T. Abe, and Z. Ogumi, *Electrochem. Solid-State Lett.*, **6**, A13 (2003).
12. S.-K. Jeong, M. Inaba, Y. Iriyama, T. Abe, and Z. Ogumi, *J. Power Sources*, **175**, 540 (2008).
13. K. Matsumoto, K. Inoue, K. Nakahara, R. Yuge, T. Noguchi, and K. Utsugi, *J. Power Sources*, **231**, 234 (2013).
14. K. Yoshida, M. Nakamura, Y. Kazue, N. Tachikawa, S. Tsuzuki, S. Seki, K. Dokko, and M. Watanabe, *J. Am. Chem. Soc.*, **133**, 13121 (2011).
15. D. W. McOwen, D. M. Seo, O. Borodin, J. Vatamanu, P. D. Boyle, and W. A. Henderson, *Energy & Environmental Science*, **7**, 416 (2014).
16. Y. Yamada, Y. Takazawa, K. Miyazaki, and T. Abe, *The Journal of Physical Chemistry C*, **114**, 11680 (2010).
17. Y. Yamada, M. Yaegashi, T. Abe, and A. Yamada, *Chem. Commun.*, **49**, 11194 (2013).
18. Y. Yamada, K. Utsui, C. H. Chiang, K. Kikuchi, K. Furukawa, and A. Yamada, *ACS Applied Materials & Interfaces*, **6**, 10892 (2014).
19. S.-K. Jeong, H.-Y. Seo, D.-H. Kim, H.-K. Han, J.-G. Kim, Y. B. Lee, Y. Iriyama, T. Abe, and Z. Ogumi, *Electrochem. Commun.*, **10**, 635 (2008).
20. L. Suo, Y.-S. Hu, H. Li, M. Armand, and L. Chen, *Nat. Commun.*, **4**, 1481 (2013).
21. M. Forsyth, H. Yoon, F. Chen, H. Zhu, D. R. MacFarlane, M. Armand, and P. C. Howlett, *J. Phys. Chem. C*, **120**, 4276 (2016).
22. E. Flores, G. Ávall, S. Jeschke, and P. Johansson, *Electrochim. Acta*, **233**, 134 (2017).
23. G. Ávall and P. Johansson, *J. Chem. Phys.*, **152**, 234104 (2020).
24. R.-S. Kühnel, D. Reber, and C. Battaglia, *ACS Energy Lett.*, **2**, 2005 (2017).
25. L. Suo et al., *Adv. Energy Mater.*, **7**, 1701189 (2017).
26. S.-D. Han, O. Borodin, D. M. Seo, Z.-B. Zhou, and W. A. Henderson, *J. Electrochem. Soc.*, **161**, A2042 (2014).
27. D. M. Seo, O. Borodin, D. Balogh, M. O'Connell, Q. Ly, S.-D. Han, S. Passerini, and W. A. Henderson, *J. Electrochem. Soc.*, **160**, A1061 (2013).
28. M. Okoshi, C.-P. Chou, and H. Nakai, *J. Phys. Chem. B*, **122**, 2600 (2018).
29. D. Brouillette, D. E. Irish, N. J. Taylor, G. Perron, M. Odziemkowski, and J. E. Desnoyers, *Phys. Chem. Chem. Phys.*, **4**, 6063 (2002).
30. D. M. Seo, O. Borodin, S.-D. Han, P. D. Boyle, and W. A. Henderson, *J. Electrochem. Soc.*, **159**, A1489 (2012).
31. H. Lundgren, J. Scheers, M. Behm, and G. Lindbergh, *J. Electrochem. Soc.*, **162**, A1334 (2015).
32. V. Nilsson, D. Bernin, D. Brandell, K. Edström, and P. Johansson, *Chem. Phys. Chem.*, **21**, 1166 (2020).
33. M. Doyle and J. Newman, *Electrochim. Acta*, **40**, 2191 (1995).
34. J. S. Newman and K. E. Thomas-Alyea, *Electrochemical Systems* (Wiley, New York) (2004).
35. M. Safari, C. Y. Kwok, and L. F. Nazar, *ACS Cent. Sci.*, **2**, 560 (2016).
36. M. McEldrew, Z. A. H. Goodwin, S. Bi, M. Z. Bazant, and A. A. Kornyshev, *J. Chem. Phys.*, **152**, 234506 (2020).
37. M. P. Allen and D. J. Tildesley, *Computer Simulation of Liquids* 2nd Edn ed. (Oxford)(Oxford University Press) p. 641 (2017).
38. O. Borodin and G. D. Smith, *J. Phys. Chem. B*, **113**, 1763 (2009).
39. P. Ganesh, D. Jiang, and P. R. C. Kent, *J. Phys. Chem. B*, **115**, 3085 (2011).
40. D. M. Seo, O. Borodin, S.-D. Han, Q. Ly, P. D. Boyle, and W. A. Henderson, *J. Electrochem. Soc.*, **159**, A553 (2012).
41. M. T. Ong, O. Verners, E. W. Draeger, A. C. T. van Duin, V. Lordi, and J. E. Pask, *J. Phys. Chem. B*, **119**, 1535 (2015).
42. O. Borodin, M. Olguin, P. Ganesh, P. R. C. Kent, J. L. Allen, and W. A. Henderson, *Phys. Chem. Chem. Phys.*, **18**, 164 (2015).
43. V. Chaban, *Chem. Phys. Lett.*, **631–632**, 1 (2015).
44. Z.-K. Tang, J. S. Tse, and L.-M. Liu, *J. Phys. Chem. Lett.*, **7**, 4795 (2016).
45. N. Kumar and J. M. Seminario, *J. Phys. Chem. C*, **120**, 16322 (2016).
46. B. Ravikumar, M. Mynam, and B. Rai, *J. Phys. Chem. C*, **122**, 8173 (2018).
47. M. T. Ong, H. Bhatia, A. G. Gyulassy, E. W. Draeger, V. Pascucci, P.-T. Bremer, V. Lordi, and J. E. Pask, *J. Phys. Chem. C*, **121**, 6589 (2017).
48. A. A. Franco, A. Rucci, D. Brandell, C. Frayret, M. Gaberscek, P. Jankowski, and P. Johansson, *Chem. Rev.*, **119**, 4569 (2019).
49. M. J. Servis, E. Martinez-Baez, and A. E. Clark, *Phys. Chem. Chem. Phys.*, **22**, 9850 (2020).
50. J.-N. Chazalviel, *Phys. Rev. A*, **42**, 7355 (1990).
51. V. Nilsson, R. Younesi, D. Brandell, K. Edström, and P. Johansson, *J. Power Sources*, **384**, 334 (2018).
52. R. Car and M. Parrinello, *Phys. Rev. Lett.*, **55**, 2471 (1985).
53. J. P. Perdew, K. Burke, and M. Ernzerhof, *Phys. Rev. Lett.*, **77**, 3865 (1996).
54. V. Nilsson, Chalmers University of Technology and Uppsala University, private correspondence (2020).
55. M. J. Frisch et al., *Gaussian* (Gaussian, Inc., Wallingford CT) 16 (2016).
56. Y. Zhao and D. G. Truhlar, *Theor. Chem. Account.*, **120**, 215 (2008).
57. J.-C. Lassègues, J. Grondin, C. Aupetit, and P. Johansson, *J. Phys. Chem. A*, **113**, 305 (2009).
58. S. Duluard, J. Grondin, J.-L. Bruneel, I. Pianet, A. Grélard, G. Campet, M.-H. Delville, and J.-C. Lassègues, *J. Raman Spectrosc.*, **39**, 627 (2008).
59. R. G. Pearson, *J. Am. Chem. Soc.*, **85**, 3533 (1963).
60. P. Johansson, S. P. Gejji, J. Tegenfeldt, and J. Lindgren, *Electrochim. Acta*, **43**, 1375 (1998).
61. V. Thangavel, O. X. Guerrero, M. Quiroga, A. M. Mikala, A. Rucci, and A. A. Franco, *Energy Storage Mater.*, **24**, 472 (2020).